TU Delft

Delft University of Technology

Document Version
Final published version

Licence
CC BY

Citation (APA)
Persky, E., Wang, X., Sala, G., van Thiel, T. C., Lesne, E., Lau, A., Cuoco, M., Gabay, M., Caviglia, A. D., & More Authors (2026). Imaging orbital Rashba induced charge transport anisotropy. *Physical Review Research*, *8*(4), Article L042008. https://doi.org/10.1103/py14-kv7p

Important note
To cite this publication, please use the final published version (if applicable).
Please check the document version above.

Copyright
In case the licence states “Dutch Copyright Act (Article 25fa)”, this publication was made available Green Open Access via the TU Delft Institutional Repository pursuant to Dutch Copyright Act (Article 25fa, the Taverne amendment). This provision does not affect copyright ownership.
Unless copyright is transferred by contract or statute, it remains with the copyright holder.

Sharing and reuse
Other than for strictly personal use, it is not permitted to download, forward or distribute the text or part of it, without the consent of the author(s) and/or copyright holder(s), unless the work is under an open content license such as Creative Commons.

Takedown policy
Please contact us and provide details if you believe this document breaches copyrights.
We will remove access to the work immediately and investigate your claim.

This work is downloaded from Delft University of Technology.

Letter

Imaging orbital Rashba induced charge transport anisotropy

Eylon Persky,[1,2] Xi Wang,[1] Giacomo Sala,[3] Thierry C. van Thiel,[4] Edouard Lesne,[4,5] Alexander Lau,[6] Mario Cuoco,[7] Marc Gabay,[8] Carmine Ortix,[9,*] Andrea D. Caviglia,[3,†] and Beena Kalisky[1,‡]

[1]*Department of Physics and Institute of Nanotechnology and Advanced Materials, Bar-Ilan University, Ramat-Gan 5290002, Israel*
[2]*Department of Applied Physics and Geballe Laboratory for Advanced Materials, Stanford University, Stanford, California 94305, USA*
[3]*Department of Quantum Matter Physics, University of Geneva, 24 Quai Ernest Ansermet, CH-1211 Geneva, Switzerland*
[4]*Kavli Institute of Nanoscience, Delft University of Technology, Lorentzweg 1, 2628CJ Delft, Netherlands*
[5]*Max Planck Institute for Chemical Physics of Solids, 01187 Dresden, Germany*
[6]*International Research Centre MagTop, Institute of Physics, Polish Academy of Sciences, Aleja Lotników 32/46, PL-02668 Warsaw, Poland*
[7]*Consiglio Nazionale delle Ricerche, CNR-SPIN, Fisciano, Italy*
[8]*Laboratoire de Physique des Solides, Universite Paris-Saclay, CNRS UMR 8502, Orsay, France*
[9]*Dipartimento di Fisica "E. R. Caianiello", Universitá di Salerno, IT-84084 Fisciano, Italy*

(Received 24 June 2025; revised 21 January 2026; accepted 27 August 2026; published 19 October 2026)

We reveal a direct orbital contribution to charge transport at the $LaAlO_3/SrTiO_3$ interface using scanning superconducting quantum interference device current imaging and global transport. Current patterns reveal conductivity anisotropy at zero field. This anisotropy correlates with the nonlinear Hall effect, pointing to a shared origin. Using a $\mathbf{k}\cdot\mathbf{p}$ model, we show that the local and global transport result from broken rotation and inversion symmetries, which give rise to anisotropic orbital Rashba coupling. Our results establish a route for probing orbital textures via purely electrical means.

DOI: 10.1103/py14-kv7p

Introduction. The multiorbital nature of oxide interfaces [1–3], combined with their low crystalline symmetry, enables a plethora of quantum phenomena, such as quantum-geometry-induced nonlinear transport [4–6] and unconventional superconductivity [7,8]. The gate tunability of these properties is particularly promising as a platform to engineer novel devices or investigate transitions between different electronic phases. One example is the orbital Hall effect (OHE) [9] and its surface counterpart, the orbital Rashba-Edelstein effect (OREE), where a charge current generates a transverse flow of orbital angular momentum. These effects are analogous to the spin Hall effect and the spin Rashba-Edelstein effect, respectively. Through this effect, the orbital degree of freedom can be used to generate and detect information [10]. Both the OREE and the OHE can be directly related to the existence of momentum-space orbital textures [11]. In noncentrosymmetric low-dimensional materials, these textures arise from a linear coupling, known as the orbital Rashba coupling [12,13], between the crystalline momentum $\mathbf{k}$ and the orbital angular momentum $\mathbf{L}$. The coupling strength can be controlled using electrostatic fields, setting the stage for a controlled generation of orbital currents. This provides a strong motivation to detect orbital textures and identify their sources in materials with low crystalline symmetry. One approach is to analyze how such couplings affect the charge transport properties of the material. For example, Rashba spin-orbit coupling (SOC) gives rise to weak antilocalization, with signatures such as positive magnetoresistance [14] and (non)linear transport due to band geometric properties [4,6,15,16]. In contrast, the signatures of orbital effects are often difficult to detect, because they are weak, or because multiple microscopic mechanisms can explain the observed experimental results. In these cases, new tools, or a combination of several probes, are required to pinpoint the cause of transport anomalies.

A notable example is the transport anisotropy in $LaAlO_3/SrTiO_3$. At low temperatures, the tetragonal distortion of $SrTiO_3$ (STO) breaks the rotational symmetry, allowing for anisotropy in the dc, zero-field charge transport. Indeed, experiments generally measure such anisotropy [17–22], but its source has been disputed. Several intrinsic mechanisms can generate anisotropy, including Fermi surface warping and the orbital Rashba coupling. The latter option, which further requires inversion symmetry breaking, is particularly interesting because it gives rise to transverse orbital currents, which are useful for device applications [23,24]. In the superconducting state, such orbital mixing could also lead to new pairing channels [25]. However, the large variability in reported results, as well as several scanning probe experiments [19,20,26–31], suggested that the origin could be extrinsic. Namely, tetragonal domains of different orientations can have different properties [29,30], or the walls

*Contact author: cortix@unisa.it
†Contact author: andrea.caviglia@unige.ch
‡Contact author: beena@biu.ac.il

Published by the American Physical Society under the terms of the Creative Commons Attribution 4.0 International license. Further distribution of this work must maintain attribution to the author(s) and the published article's title, journal citation, and DOI.

between the structural domains could host highly conducting quasi-one-dimensional channels [32–34] that manifest as anisotropy in the global transport measurement. Thus, a key open question is whether the anisotropy reflects intrinsic, domain-dependent conductivity or conduction along the domain walls. Determining the origin of anisotropy is crucial to interpreting quantum transport measurements in $SrTiO_3$-based interfaces, and for harnessing their properties for device applications.

In this work, we use a combination of global transport measurements, local current imaging, and theoretical analysis to associate the origin of transport anisotropy in (111)-oriented $LaAlO_3/SrTiO_3$ interface with the orbital Rashba coupling. First, we locally probe the current flow at the interface and show direct and unambiguous evidence that the anisotropy is an intrinsic property of the interface. In particular, we observe geometry-dependent current-density modulation, which is inconsistent with a fixed high-conductivity channel at domain walls and instead indicates a domain-dependent conductivity tensor. Second, we measure the nonlinear Hall effect, whose presence is a direct indicator of inversion symmetry breaking. We find a correlation between the temperature dependence of the two effects, which motivates considering a common microscopic origin, while not by itself establishing one. Finally, we interpret these results using a $\mathbf{k}\cdot\mathbf{p}$ model of the band structure, which allows us to identify the anisotropic orbital Rashba coupling—a linear-in-momentum, anisotropic mixing of the t_{2g} orbitals—as the leading term responsible for both effects. Our results provide a platform for exploring orbital effects and controlling the orbital degree of freedom in various systems.

Experimental details.

a. Sample growth and device fabrication. To synthesize the $LaAlO_3/SrTiO_3$ heterostructure, a commercially available (111) $SrTiO_3$ substrate with a Ti-rich surface was pasted onto a metal holder and heated to 740 °C, at a rate of 15 °C min^{-1} in an O_2 pressure of 6×10^{-5} mbar. An 11 unit cell thick $LaAlO_3$ layer was subsequently grown through pulsed-laser deposition, using a 248 nm KrF excimer laser at a 1 Hz repetition rate and a fluence of 1 J cm^{-2}. The sample surface was monitored during the growth using *in situ* reflection high-energy electron diffraction technique.

Device geometries were defined by rf sputtering a HfO_2 hard mask in areas meant to remain insulating, prior to the growth of the $LaAlO_3$ layer. The hard mask was defined by electron-beam lithography, using a double-layer poly(methyl methacrylate) lift-off resist stack.

b. Imaging currents with scanning superconducting quantum interference device (SQUID) microscopy. The sample was glued on a conductive surface and electrical contacts made by ultrasonic wire bonding. A backgate voltage was applied between the interface and the metallic sample holder. To locally measure the current density, an alternating current (34 μA RMS, frequency 1163 Hz for the triangle-shaped device shown in Fig. 1; 40 μA RMS, frequency 1009 Hz for the device shown in Figs. S9 and S10 of the Supplemental Material [36]) was applied to the $LaAlO_3/SrTiO_3$ device. The sample was scanned over a planar SQUID sensor with a 0.8 μm diameter pickup loop [35]. The sensor-sample distance was kept at 1 μm. The magnetic flux due to the current flow was recorded using a lock-in amplifier.

c. Electrical transport measurements. The nonlinear Hall effect was measured on a Hall cross device fabricated on the same sample as used for the SQUID imaging. The sample was anchored to a chip carrier by electrically and thermally-conductive Ag-based epoxy, and the device was electrically contacted with Al wire bonds. Four-probe measurements were performed in a liquid He^4 cryostat at variable temperatures and magnetic fields (applied in the sample plane parallel to the electric current direction). Commercial lock-in amplifiers were used to apply an alternate current $I = 50\,\mu\mathrm{A}$ at a frequency $f = \omega/2\pi = 17.7\,\mathrm{Hz}$ and detect the transverse first and second harmonic voltages while sweeping the magnetic field. A dc backgate voltage was applied to tune the electronic density and mobility. The measured nonlinear Hall voltage was symmetrized and antisymmetrized with respect to the magnetic field B to isolate distinct effects [4]. The nonlinear conductivity shown in Figs. 2(c) and S7 of the Supplemental Material [36] corresponds to the B-symmetric component.

Results.

a. Intrinsic anisotropy in (111) $LaAlO_3/SrTiO_3$. To distinguish between intrinsic and extrinsic origins of transport anisotropy, we used a local probe, a scanning SQUID, to directly image the current flow at the interface. Scanning SQUID was previously used to study (001)-based interfaces, revealing that current density is spatially inhomogeneous, and that the inhomogeneity is correlated with the tetragonal domain structure of the $SrTiO_3$ substrate [26]. While these observations might point to an extrinsic source—the network of domains or domain walls—this determination cannot be made based on existing data. Specifically, it was difficult to distinguish between enhanced current density on entire domains versus domain boundaries, and to relate these to the components of the conductivity tensor. Here, we study the (111)-oriented interface, in which we found that domains tend to be wider, and the tiling rules of the domains enable us to determine their orientations unambiguously.

Figure 1 shows results from a triangle patterned (111)-oriented $LaAlO_3/SrTiO_3$ device [36]. We observed current density modulations [Fig. 1(b)], across the device. The modulations changed after a thermal cycle above 105 K, confirming that they originate from the STO tetragonal domains (Fig. S1 in the Supplemental Material [36]). Based on the tiling rules, we determined the orientation of the domains to be along the [100] and [010] axes. The modulations were over 10 μm wide strips that terminate at needlelike shapes. When needle patterns form, the domain wall energetics result in a diverging characteristic domain size [37], disfavoring the formation of small domains. As a result, the observation of modulations over such patterns allows us to conclude that the current modulation occurs over entire domains, rather than a dense network of walls that cannot be resolved by our sensor. The modulations reveal a surprising dependence on the device geometry: On the left side of the triangle, the current density along $[11\bar{2}]$ is larger on X domains than on Y domains but lower on the right side. The change coincides with a reflection of $\mathbf{J}$ with respect to the $[11\bar{2}]$ crystallographic direction. This relationship between the current direction and the modulation has not been previously reported in the (001) interface. We

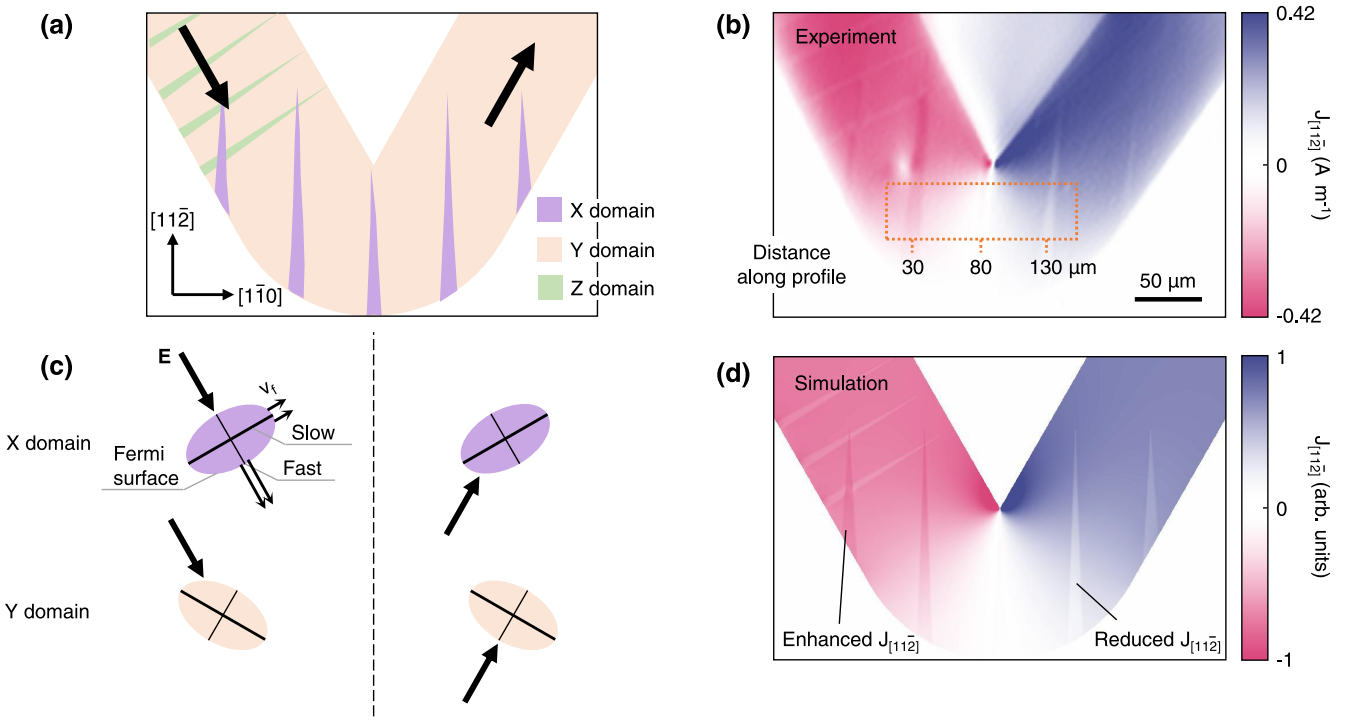


FIG. 1. Modulation reversal upon reflection of the current flow. (a) Schematic of a triangle-shaped device with an X-Y domain pattern. The current density is reflected around the [11$\bar{2}$] direction upon flowing across the device. (b) A scanning SQUID image of the current flow in a (111)-oriented device. The current is modulated over the domain pattern: On the left side of the device, current density on X domains is larger than on Y domains. This trend is reversed on the right side of the device, coinciding with a reflection of the overall current density. The modulation strength is about 10%–20%. (c) Schematic of the Fermi surface at the X and Y domains, showing the direction of the electric field on the two sides of the device. On the left, the electric field is aligned with the fast direction on X domains, resulting in increased current density. This is reversed on the right side of the device. (d) Simulated current density map of the device, where an anisotropic conductivity tensor was introduced in order to account for the reversed modulations.

thus associate the modulations with a change in the properties of the X and Y domains, rather than a domain-boundary effect. Figures S2–S4 of the Supplemental Material [36] show data from three additional devices with various geometries and domain patterns.

To understand the difference between the (001) and (111) interfaces, we note that at (001) interfaces, (001)-oriented domains (Z domains) have a $\mathcal{C}_{4v}$ symmetry, while (100) and (010) domains (X, Y domains) have $\mathcal{C}_{2v}$ symmetry. Therefore, in (001) interfaces, the conductivity of Z domains is intrinsically isotropic and is described by a single scalar. For X and Y domains, the conductivity tensor has a symmetry-allowed anisotropy, but it is diagonal with respect to the (100) and (010) directions. The situation changes in (111)-oriented interfaces. All domains have the same crystalline symmetry group, $\mathcal{C}_s$, which admits an anisotropic conductivity tensor with principal directions that do not coincide with the crystallographic directions. Denote the current density as the two-dimensional (2D) vector

$$\mathbf{J} = \begin{pmatrix} J_{[1\bar{1}0]} \\ J_{[11\bar{2}]} \end{pmatrix}. \tag{1}$$

The conductivity tensor for Z domains is anisotropic but diagonal,

$$\sigma^Z = \begin{pmatrix} \sigma_{xx} & 0 \\ 0 & \sigma_{yy} \end{pmatrix}, \tag{2}$$

while the X and Y domain conductivities are related by a 120° rotation,

$$\sigma^{X,Y} = \frac{1}{4}\begin{pmatrix} \sigma_{xx} + 3\sigma_{yy} & \pm\sqrt{3}(\sigma_{xx} - \sigma_{yy}) \\ \pm\sqrt{3}(\sigma_{xx} - \sigma_{yy}) & \sigma_{yy} + 3\sigma_{xx} \end{pmatrix}. \tag{3}$$

Note that the off-diagonal elements are nonzero (in zero magnetic field) only if the conductivity is anisotropic ($\sigma_{xx} \neq \sigma_{yy}$).

The off-diagonal components of the conductivity are at the origin of the reversed modulations observed in the data. In Fig. 1(c), we schematically show an anisotropic Fermi surface with corresponding direction-dependent Fermi velocities that yield a fast and a slow direction. The current density **J** is increased when the electric field is aligned with the fast direction of the Fermi surface, which causes the modulations. On the left side of the device, this alignment is greater in X domains. As the current flow is reflected about the [11$\bar{2}$] direction, due to the triangle shape of the device, **E** is aligned with the fast direction in the Y domains, thus reversing the current density modulation. Figure 1(d) shows finite element simulations [36] of the current density in such geometry, which confirm that the modulation trends are reversed. Furthermore, domains with different (but isotropic) conductivity would lead to modulations that do not reverse sign upon reflection of the device [36]. Thus, observing this change of sign is a

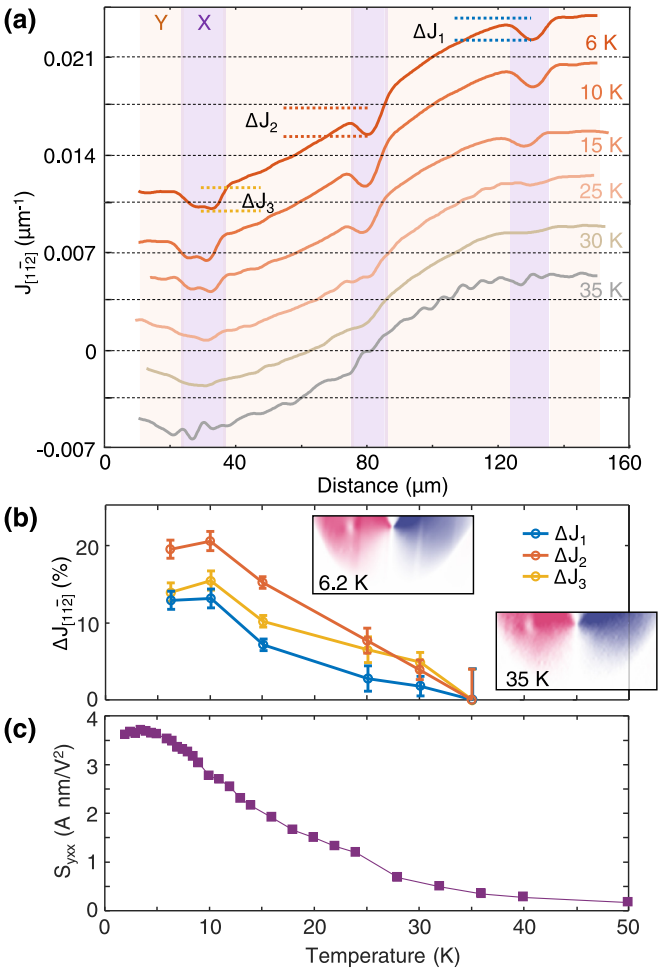


FIG. 2. Temperature and carrier density dependence of the anisotropy. (a) Averaged linecut in the dashed square along the [11$\bar{2}$] direction in Fig. 1(b) from 6 to 35 K. The relative positions of X domains in the averaged linecut are marked near the dashed square. The profiles are vertically offset for clarity relative to the unshifted 35 K profile. In the unshifted data, the profiles cross zero when the current reverses direction. This modulation is 10%–20% of the averaged total current density |J| at 6 K, which is calculated as 0.01 μm^{-1}. The current densities are normalized by the applied current. (b) Temperature dependence of the current density modulations shown in panel (a). The modulation of current density decreases with temperature and disappears near 35 K. Insets: current density maps at 6 and 35 K. Error bars represent the current reconstruction systematic noise for each measurement temperature. (c) Temperature dependence of the nonlinear conductivity, measured at zero magnetic field on a four-probe device fabricated on the same sample, showing similar onset temperature to the anisotropy.

direct measure of the intrinsic conductivity anisotropy of an individual domain.

b. Correlation between anisotropy and inversion symmetry breaking. To investigate the origin of the anisotropy, we studied the temperature dependence of the modulations. In Fig. 2(a), we show linecuts of $J_{[11\bar{2}]}$ taken on the triangle-shaped device at different temperatures. From these linecuts, we quantify the current density modulation $\Delta J_{[11\bar{2}]}$ on each X domain as the difference from the density on the nearest Y domain. Figure 2(b) shows $\Delta J_{[11\bar{2}]}$ decreasing with increasing temperature, until it is smaller than the noise level at 35 K. Although the signal to noise is limited near the crossover, our sensitivity can still give an upper limit of $\Delta J_{[11\bar{2}]}$ around 5% [Fig. 2(b), corresponding to 0.3 μA modulated current flowing through the X domain]. This temperature dependence is consistent with previous observations on the (001) interface [26,38]. It is important to note that even though the domains exist already at 105 K, and the crystalline symmetry allows anisotropy to exist below 105 K, it is not observed in the range $35 < T < 105$, suggesting there is another mechanism that generates or enhances the anisotropy at lower temperatures.

There are several possible mechanisms. Scattering can smear the effect at elevated temperatures, explaining the gradual change in the signal. In $SrTiO_3$, the scattering could be suppressed at low temperatures due to the large dielectric constant. Alternatively, the appearance of modulations only below 35 K can suggest that the modulations are caused by a structural change occurring at this temperature. Bulk $SrTiO_3$ shows an increased dielectric permittivity below 40 K, signaling an incipient ferroelectric state [39]. This quantum paraelectric phase significantly enhances the inversion symmetry breaking that is already present at the interface [40]. This observation suggests that, while the relevant symmetries are already broken at higher temperatures, an additional low-temperature ingredient enhances the manifestation of transport anisotropy. This motivates us to search for transport signatures that are directly sensitive to inversion symmetry breaking and could help identify the microscopic mechanism responsible for the enhanced anisotropy at low temperatures.

To understand the source of the anisotropy, we further studied the symmetry of the system by measuring the nonlinear Hall effect. Observing nonlinear transport is a direct consequence of inversion symmetry breaking. Furthermore, previous work on oxide interfaces, which studied the magnetic field dependence of the nonlinear Hall [4], associated it with a Berry curvature dipole, which indicates the presence of an orbital Rashba coupling. Since the triangle-shaped device geometry is incompatible with Hall measurements, we used a separate device with a four-probe geometry fabricated on the same sample for the nonlinear transport (Fig. S7 in the Supplemental Material [36]). We found that it onsets at 40 K [Fig. 2(c)], and a different sample shows the same onset temperature of nonlinear conductivity [4]. Remarkably, both the linear conductivity anisotropy and the nonlinear Hall conductivity onset at the same temperature, even though the corresponding crystalline symmetries (rotation and inversion) are already broken at much higher temperatures. The similar onset temperatures of the linear conductivity anisotropy and the nonlinear Hall response point to a correlation between the two effects. While this does not by itself establish a common microscopic origin, it motivates considering mechanisms that can simultaneously affect both inversion and rotational symmetry breaking.

c. $\mathbf{k}\cdot\mathbf{p}$ *model and sources of anisotropy.* We use a $\mathbf{k}\cdot\mathbf{p}$ model to analyze the symmetry-allowed terms and their contribution to the transport anisotropy. Above 105 K, the system retains its trigonal symmetry and belongs to the $\mathcal{C}_{3v}$ symmetry group. At zero magnetic field, the spin degree of freedom does not contribute to the linear conductivity [41]. We therefore

consider a spinless Hamiltonian, which contains the following symmetry-allowed terms: (1) Splitting between the a_{1g} singlet and the e_g^π doublet due to the trigonal field and (2) $|\mathbf{k}|^2$ terms that account for the trigonal Fermi surface warping. They give rise to an orbital-dependent effective mass, as observed in ARPES experiments [42], and (3) k-linear terms that are allowed by the broken inversion symmetry. These terms, which are proportional to $\mathbf{k}\cdot\mathbf{L}$, where $\mathbf{L}$ are the angular momentum matrices, are the orbital Rashba coupling. They mix the orbital bands and give rise to transverse orbital currents and Berry curvature dipoles.

Below 105 K, the rotational symmetry is broken, reducing the symmetry group to $\mathcal{C}_s$ and enabling a plethora of new terms in the Hamiltonian. These terms can be casted into three categories [36]: (4) splitting of the e_g^π bands, (5) an anisotropic and orbital-dependent effective mass (terms proportional to k_x^2 or k_y^2), and [43–46] (6) an anisotropic orbital Rashba coupling (linear in k_x and k_y).

The correlation between the nonlinear Hall effect (broken inversion) and the anisotropic linear transport (broken rotation) suggests that the two effects are intertwined. Particularly, we expect the orbital Rashba terms to change strongly at 40 K, as indicated by the nonlinear Hall. Figure 3(a) shows the band structure obtained by fitting to photoemission data from a (111) $SrTiO_3$ surface [42]. We note that epitaxial strain from the $LaAlO_3$ layer may cause large changes to the tight-binding parameters compared to the bare surface. However, the structural changes decay to bulk values within 2 nm from the interface [47], whereas at low temperature the two-dimensional electron gas extends tens of nanometers into the $SrTiO_3$ side [48], suggesting that the bulk or bare surface values are realistic. Since the ARPES data fit well to an isotropic model, they provide upper bounds on the contributions from the $\mathcal{C}_s$ terms discussed above. To account for the tetragonal distortion, we only include a small splitting (1 meV) of the e_g^π bands. Figures 3(a)–3(c) show the resulting band structure and the corresponding Fermi surfaces at carrier densities relevant to our experiment (Fig. S7 in the Supplemental Material [36]). The band structure has several important features. First, at low densities it is dominated by the orbital Rashba coupling, which gives rise to the two shifted parabolic features in the lowest bands. Note that at these low energies, the Fermi surface does not show significant tetragonal warping [Fig. 3(b)], but is strongly anisotropic. At higher energies, the warping becomes significant. Notably, the anisotropy in the higher e_g^π bands is opposite to that of the a_{1g} band [Fig. 3(a)]. Correspondingly, the transport anisotropy computed using the Boltzmann formalism [36] is nonmonotonic and is stronger at low densities [Fig. 3(e)]. This matches the behavior observed in experiment over the smaller (experimentally attainable) range of densities (Fig. S6 in the Supplemental Material [36]).

To assess the contribution of Fermi surface warping to the transport anisotropy, we repeated the calculation without including the orbital Rashba effect. The resulting anisotropy was zero at low carrier densities and varied monotonically and quadratically with increasing densities, reflecting the contributions from the quadratic terms. These results indicate that the tetragonal splitting of the e_g^π bands on its own is not

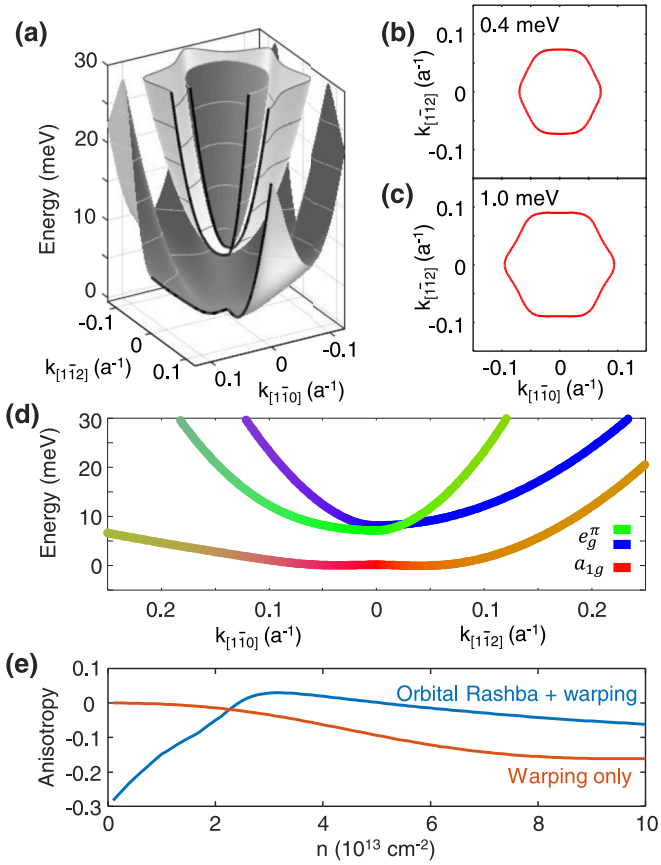


FIG. 3. The anisotropic band structures of (111) $LaAlO_3/SrTiO_3$, and carrier density dependence of the anisotropy. (a) The band structure calculated from an effective $\mathbf{k}\cdot\mathbf{p}$ model, showing effects of the orbital Rashba coupling (lateral splitting of the lowest band), Fermi surface warping (flowerlike shape at higher energies), and the tetragonal splitting of the e_g^π bands. The unit of quasimomentum is the inversed lattice constant a^{-1}. (b), (c) The Fermi surfaces 0.4 and 1 meV, showing the anisotropy at low energies, where the band structure is still dominated by the linear (Rashba) terms. (d) The profiles of the black outlines in panel (a) show the anisotropy of the band structure. (e) Calculated anisotropy as a function of the carrier density with and without including the orbital Rashba coupling.

sufficient to explain the anisotropy observed in the experiment. While an anisotropic quadratic (mass) term is allowed, and can result in a nonmonotonic dependence on the carrier density, the combination of the SQUID images, nonlinear Hall effect, temperature, and gate dependence indicate that the anisotropy is correlated with the broken inversion symmetry, consistent with the calculations we present, which indicate that the orbital Rashba coupling greatly enhances the anisotropy at low energies.

Discussion. In this work, we show that momentum-space orbital textures can be probed by charge transport by exploiting reduced crystalline symmetry. Specifically, the absence of rotational symmetry gives rise to intraatomic contributions to the orbital Hall effect, which are absent in more symmetric environments. In this low-symmetry setting, transport anisotropy becomes a direct electrical proxy for the underlying orbital texture and associated orbital currents. We

developed an approach to explore the anisotropy by extracting it from local measurements of the current density, and demonstrated it on (111) $LaAlO_3/SrTiO_3$.

In LAO/STO, spin-orbit coupling plays an important role in determining the band structure and electronic behavior [49–53]. The zero-field intrinsic anisotropy uncovered here demonstrates our ability to separate the orbital and spin contributions to transport and identify new features in the band structure. Furthermore, we identify the origin of the previously reported current-density modulations in LAO/STO [19,20,26,27,31,32], as domain-dependent anisotropic conductivity (with principal axes rotated across domains), rather than conduction confined to the domain walls.

More generally, our results indicate that by choosing the appropriate crystalline symmetry, orbital currents can be identified by measuring transport anisotropy. This task can be accomplished via various local techniques [54–58] and also through measurements of the global transport anisotropy. Uniquely identifying orbital Hall currents, for example, has been a challenging task because their signatures are similar to spin Hall currents, and therefore limited to systems with low spin-orbit coupling [59,60]. Our approach offers a way to disentangle the spin and orbital contributions, thereby allowing the study of orbital phenomena in materials with strong SOC.

Finally, we note that the orbital effects we observed in $LaAlO_3/SrTiO_3$ are closely associated with the low-temperature transitions of $SrTiO_3$. However, a similar low-symmetry structure could be engineered at room temperature by breaking the rotation and inversion symmetries using epitaxial strain and ferroelectric layers. This engineering of orbital-induced anisotropy is relevant not only to complex oxide interfaces. It applies to other orbitronics material candidates, including light and heavy elemental metals and van der Waals heterostructures. For example, while many van der Waals materials nominally have sixfold rotation symmetry, encapsulation and device topology break the rotation and inversion symmetry [61–63], in principle allowing the same orbital effects observed here. Similarly, the use of $SrTiO_3$ as a screening dielectric [64,65] extends the effects to the device layers to which the $SrTiO_3$ substrate is proximitized. Local measurements of anisotropy are particularly helpful in such systems, as it is often challenging to determine the transport anisotropy from global measurements. The theoretical model and experimental techniques presented here provide an effective platform to characterize the orbital degrees of freedom in these systems.

Acknowledgments. E.P., X.W., and B.K. were supported by the European Research Council Grant No. ERC-2019-COG-866236, the Israeli Science Foundation, Grant No. ISF-228/22, COST (European Cooperation in Science and Technology) Action CA21144, and the Pazy Research Foundation Grant No. 107-2018. G.S. acknowledges support from the Swiss National Science Foundation (Grant No. PZ00P2_223542). A.L. was supported by a Marie Skłodowska-Curie Individual Fellowship under grant MagTopCSL (ID 101029345) and by the Foundation for Polish Science through the IRA Programme cofinanced by EU within SG OP. C.O. acknowledges support from a VIDI grant (Project No. 680-47-543) financed by the Netherlands Organization for Scientific Research (NWO). E.L. acknowledges funding from the EU Horizon 2020 Research and Innovation Programme under the Marie Skłodowska-Curie Grant Agreement No. 707404.

Data availability. The data that support the findings of this article are available upon reasonable request.

[1] Y.-Y. Pai, A. Tylan-Tyler, P. Irvin, and J. Levy, Physics of $SrTiO_3$-based heterostructures and nanostructures: A review, Rep. Prog. Phys. **81**, 036503 (2018).

[2] H. Y. Hwang, Y. Iwasa, M. Kawasaki, B. Keimer, N. Nagaosa, and Y. Tokura, Emergent phenomena at oxide interfaces, Nat. Mater. **11**, 103 (2012).

[3] C. Ahn, A. Cavalleri, A. Georges, S. Ismail-Beigi, A. J. Millis, and J.-M. Triscone, Designing and controlling the properties of transition metal oxide quantum materials, Nat. Mater. **20**, 1462 (2021).

[4] E. Lesne, Y. G. Sağlam, R. Battilomo, M. T. Mercaldo, T. C. van Thiel, U. Filippozzi, C. Noce, M. Cuoco, G. A. Steele, C. Ortix, and A. D. Caviglia, Designing spin and orbital sources of Berry curvature at oxide interfaces, Nat. Mater. **22**, 576 (2023).

[5] M. T. Mercaldo, C. Noce, A. D. Caviglia, M. Cuoco, and C. Ortix, Orbital design of Berry curvature: Pinch points and giant dipoles induced by crystal fields, npj Quantum Mater. **8**, 12 (2023).

[6] G. Sala, M. T. Mercaldo, K. Domi, S. Gariglio, M. Cuoco, C. Ortix, and A. D. Caviglia, The quantum metric of electrons with spin-momentum locking, Science **389**, 822 (2025).

[7] N. Reyren, S. Thiel, A. D. Caviglia, L. F. Kourkoutis, G. Hammerl, C. Richter, C. W. Schneider, T. Kopp, A.-S. Rüetschi, D. Jaccard, M. Gabay, D. A. Muller, J.-M. Triscone, and J. Mannhart, Superconducting interfaces between insulating oxides, Science **317**, 1196 (2007).

[8] A. D. Caviglia, S. Gariglio, N. Reyren, D. Jaccard, T. Schneider, M. Gabay, S. Thiel, G. Hammerl, J. Mannhart, and J.-M. Triscone, Electric field control of the $LaAlO_3/SrTiO_3$ interface ground state, Nature (London) **456**, 624 (2008).

[9] B. A. Bernevig, T. L. Hughes, and S.-C. Zhang, Orbitronics: The intrinsic orbital current in *p*-doped silicon, Phys. Rev. Lett. **95**, 066601 (2005).

[10] D. Go, D. Jo, H.-W. Lee, M. Kläui, and Y. Mokrousov, Orbitronics: Orbital currents in solids, Europhys. Lett. **135**, 37001 (2021).

[11] D. Go, D. Jo, C. Kim, and H.-W. Lee, Intrinsic spin and orbital Hall effects from orbital texture, Phys. Rev. Lett. **121**, 086602 (2018).

[12] S. R. Park, C. H. Kim, J. Yu, J. H. Han, and C. Kim, Orbital-angular-momentum based origin of Rashba-type surface band splitting, Phys. Rev. Lett. **107**, 156803 (2011).

[13] V. Sunko, H. Rosner, P. Kushwaha, S. Khim, F. Mazzola, L. Bawden, O. J. Clark, J. M. Riley, D. Kasinathan, M. W. Haverkort, T. K. Kim, M. Hoesch, J. Fujii, I. Vobornik, A. P. Mackenzie, and P. D. C. King, Maximal Rashba-like spin

splitting via kinetic-energy-coupled inversion-symmetry breaking, Nature (London) **549**, 492 (2017).

[14] S. Hikami, A. I. Larkin, and Y. Nagaoka, Spin-orbit interaction and magnetoresistance in the two dimensional random system, Prog. Theor. Phys. **63**, 707 (1980).

[15] J. E. Moore and J. Orenstein, Confinement-induced Berry phase and helicity-dependent photocurrents, Phys. Rev. Lett. **105**, 026805 (2010).

[16] I. Sodemann and L. Fu, Quantum nonlinear Hall effect induced by Berry curvature dipole in time-reversal invariant materials, Phys. Rev. Lett. **115**, 216806 (2015).

[17] M. Ben Shalom, C. W. Tai, Y. Lereah, M. Sachs, E. Levy, D. Rakhmilevitch, A. Palevski, and Y. Dagan, Anisotropic magnetotransport at the $LaAlO_3/SrTiO_3$ interface, Phys. Rev. B **80**, 140403(R) (2009).

[18] A. Annadi, Z. Huang, K. Gopinadhan, X. R. Wang, A. Srivastava, Z. Q. Liu, H. H. Ma, T. P. Sarkar, T. Venkatesan, and Ariando, Fourfold oscillation in anisotropic magnetoresistance and planar Hall effect at the $LaAlO_3/SrTiO_3$ heterointerfaces: Effect of carrier confinement and electric field on magnetic interactions, Phys. Rev. B **87**, 201102(R) (2013).

[19] Y. Frenkel, N. Haham, Y. Shperber, C. Bell, Y. Xie, Z. Chen, Y. Hikita, H. Y. Hwang, and B. Kalisky, Anisotropic transport at the $LaAlO_3/SrTiO_3$ interface explained by microscopic imaging of channel-flow over $SrTiO_3$ domains, ACS Appl. Mater. Interfaces **8**, 12514 (2016).

[20] N. J. Goble, R. Akrobetu, H. Zaid, S. Sucharitakul, M.-H. Berger, A. Sehirlioglu, and X. P. A. Gao, Anisotropic electrical resistance in mesoscopic $LaAlO_3/SrTiO_3$ devices with individual domain walls, Sci. Rep. **7**, 44361 (2017).

[21] P. W. Krantz and V. Chandrasekhar, Observation of zero-field transverse resistance in $AlO_x/SrTiO_3$ interface devices, Phys. Rev. Lett. **127**, 036801 (2021).

[22] M. S. Prasad and G. Schmidt, Anisotropic magnetotransport in $LaAlO_3/SrTiO_3$ nanostructures, Phys. Rev. B **104**, 054115 (2021).

[23] D. Go, D. Jo, T. Gao, K. Ando, S. Blügel, H.-W. Lee, and Y. Mokrousov, Orbital Rashba effect in a surface-oxidized Cu film, Phys. Rev. B **103**, L121113 (2021).

[24] R. B. Atencia, A. Agarwal, and D. Culcer, Orbital angular momentum of Bloch electrons: Equilibrium formulation, magneto-electric phenomena, and the orbital Hall effect, Adv. Phys. X **9**, 2371972 (2024).

[25] M. T. Mercaldo, C. Ortix, and M. Cuoco, High orbital-moment Cooper pairs by crystalline symmetry breaking, Adv. Quantum Technol. **6**, 2300081 (2023).

[26] B. Kalisky, E. M. Spanton, H. Noad, J. R. Kirtley, K. C. Nowack, C. Bell, H. K. Sato, M. Hosoda, Y. Xie, Y. Hikita, C. Woltmann, G. Pfanzelt, R. Jany, C. Richter, H. Y. Hwang, J. Mannhart, and K. A. Moler, Locally enhanced conductivity due to the tetragonal domain structure in $LaAlO_3/SrTiO_3$ heterointerfaces, Nat. Mater. **12**, 1091 (2013).

[27] M. Honig, J. A. Sulpizio, J. Drori, A. Joshua, E. Zeldov, and S. Ilani, Local electrostatic imaging of striped domain order in $LaAlO_3/SrTiO_3$, Nat. Mater. **12**, 1112 (2013).

[28] H. J. H. Ma, S. Scharinger, S. W. Zeng, D. Kohlberger, M. Lange, A. Stöhr, X. R. Wang, T. Venkatesan, R. Kleiner, J. F. Scott, J. M. D. Coey, D. Koelle, and Ariando, Local electrical imaging of tetragonal domains and field-induced ferroelectric twin walls in conducting $SrTiO_3$, Phys. Rev. Lett. **116**, 257601 (2016).

[29] H. Noad, E. M. Spanton, K. C. Nowack, H. Inoue, M. Kim, T. A. Merz, C. Bell, Y. Hikita, R. Xu, W. Liu, A. Vailionis, H. Y. Hwang, and K. A. Moler, Variation in superconducting transition temperature due to tetragonal domains in two-dimensionally doped $SrTiO_3$, Phys. Rev. B **94**, 174516 (2016).

[30] S. Wissberg and B. Kalisky, Large-scale modulation in the superconducting properties of thin films due to domains in the $SrTiO_3$ substrate, Phys. Rev. B **95**, 144510 (2017).

[31] E. Persky, N. Vardi, A. M. R. V. L. Monteiro, T. C. van Thiel, H. Yoon, Y. Xie, B. Fauqué, A. D. Caviglia, H. Y. Hwang, K. Behnia, J. Ruhman, and B. Kalisky, Non-universal current flow near the metal-insulator transition in an oxide interface, Nat. Commun. **12**, 3311 (2021).

[32] Y. Frenkel, N. Haham, Y. Shperber, C. Bell, Y. Xie, Z. Chen, Y. Hikita, H. Y. Hwang, E. K. H. Salje, and B. Kalisky, Imaging and tuning polarity at $SrTiO_3$ domain walls, Nat. Mater. **16**, 1203 (2017).

[33] G. Cheng, A. Annadi, S. Lu, H. Lee, J.-W. Lee, M. Huang, C.-B. Eom, P. Irvin, and J. Levy, Shubnikov–de Haas–like quantum oscillations in artificial one-dimensional $LaAlO_3/SrTiO_3$ electron channels, Phys. Rev. Lett. **120**, 076801 (2018).

[34] Y.-Y. Pai, H. Lee, J.-W. Lee, A. Annadi, G. Cheng, S. Lu, M. Tomczyk, M. Huang, C.-B. Eom, P. Irvin, and J. Levy, One-dimensional nature of superconductivity at the $LaAlO_3/SrTiO_3$ interface, Phys. Rev. Lett. **120**, 147001 (2018).

[35] M. E. Huber, N. C. Koshnick, H. Bluhm, L. J. Archuleta, T. Azua, P. G. Björnsson, B. W. Gardner, S. T. Halloran, E. A. Lucero, and K. A. Moler, Gradiometric micro-squid susceptometer for scanning measurements of mesoscopic samples, Rev. Sci. Instrum. **79**, 053704 (2008).

[36] See Supplemental Material at https://link.aps.org/supplemental/10.1103/py14-kv7p for more details, and which includes Refs. [66,67],

[37] R. J. Harrison and E. K. H. Salje, Ferroic switching, avalanches, and the Larkin length: Needle domains in $LaAlO_3$, Appl. Phys. Lett. **99**, 151915 (2011).

[38] Y. Frenkel, Y. Xie, H. Y. Hwang, and B. Kalisky, Magnetism and conductivity along structural domain walls of $SrTiO_3$, J. Supercond. Novel Magn. **33**, 195 (2020).

[39] K. A. Müller and H. Burkard, $SrTiO_3$: An intrinsic quantum paraelectric below 4 K, Phys. Rev. B **19**, 3593 (1979).

[40] H.-B. Zhang and M. Alexe, Interfacial symmetry-breaking effects in the quantum paraelectric $SrTiO_3$, Phys. Rev. Appl. **19**, 014028 (2023).

[41] V. Brosco, L. Benfatto, E. Cappelluti, and C. Grimaldi, Unconventional dc transport in Rashba electron gases, Phys. Rev. Lett. **116**, 166602 (2016).

[42] T. C. Rödel, C. Bareille, F. Fortuna, C. Baumier, F. Bertran, P. Le Fèvre, M. Gabay, O. Hijano Cubelos, M. J. Rozenberg, T. Maroutian, P. Lecoeur, and A. F. Santander-Syro, Orientational tuning of the Fermi sea of confined electrons at the $SrTiO_3$ (110) and (111) surfaces, Phys. Rev. Appl. **1**, 051002(R) (2014).

[43] P. S. Bednyakov, T. Sluka, A. K. Tagantsev, D. Damjanovic, and N. Setter, Formation of charged ferroelectric domain walls with controlled periodicity, Sci. Rep. **5**, 15819 (2015).

[44] S. McKeown Walker, A. de la Torre, F. Y. Bruno, A. Tamai, T. K. Kim, M. Hoesch, M. Shi, M. S. Bahramy, P. D. C. King,

and F. Baumberger, Control of a two-dimensional electron gas on $SrTiO_3$(111) by atomic oxygen, Phys. Rev. Lett. **113**, 177601 (2014).

[45] A. F. Santander-Syro, C. Bareille, F. Fortuna, O. Copie, M. Gabay, F. Bertran, A. Taleb-Ibrahimi, P. Le Fèvre, G. Herranz, N. Reyren, M. Bibes, A. Barthélémy, P. Lecoeur, J. Guevara, and M. J. Rozenberg, Orbital symmetry reconstruction and strong mass renormalization in the two-dimensional electron gas at the surface of $KTaO_3$, Phys. Rev. B **86**, 121107(R) (2012).

[46] P. D. C. King, R. H. He, T. Eknapakul, P. Buaphet, S.-K. Mo, Y. Kaneko, S. Harashima, Y. Hikita, M. S. Bahramy, C. Bell, Z. Hussain, Y. Tokura, Z.-X. Shen, H. Y. Hwang, F. Baumberger, and W. Meevasana, Subband structure of a two-dimensional electron gas formed at the polar surface of the strong spin-orbit perovskite $KTaO_3$, Phys. Rev. Lett. **108**, 117602 (2012).

[47] P. W. Lee, V. N. Singh, G. Y. Guo, H.-J. Liu, J.-C. Lin, Y.-H. Chu, C. H. Chen, and M.-W. Chu, Hidden lattice instabilities as origin of the conductive interface between insulating $LaAlO_3$ and $SrTiO_3$, Nat. Commun. **7**, 12773 (2016).

[48] O. Copie, V. Garcia, C. Bödefeld, C. Carrétéro, M. Bibes, G. Herranz, E. Jacquet, J.-L. Maurice, B. Vinter, S. Fusil, K. Bouzehouane, H. Jaffrès, and A. Barthélémy, Towards two-dimensional metallic behavior at $LaAlO_3/SrTiO_3$ interfaces, Phys. Rev. Lett. **102**, 216804 (2009).

[49] A. D. Caviglia, M. Gabay, S. Gariglio, N. Reyren, C. Cancellieri, and J.-M. Triscone, Tunable Rashba spin-orbit interaction at oxide interfaces, Phys. Rev. Lett. **104**, 126803 (2010).

[50] M. Ben Shalom, M. Sachs, D. Rakhmilevitch, A. Palevski, and Y. Dagan, Tuning spin-orbit coupling and superconductivity at the $SrTiO_3/LaAlO_3$ interface: A magnetotransport study, Phys. Rev. Lett. **104**, 126802 (2010).

[51] A. Joshua, S. Pecker, J. Ruhman, E. Altman, and S. Ilani, A universal critical density underlying the physics of electrons at the $LaAlO_3/SrTiO_3$ interface, Nat. Commun. **3**, 1129 (2012).

[52] P. K. Rout, E. Maniv, and Y. Dagan, Link between the superconducting dome and spin-orbit interaction in the (111) $LaAlO_3/SrTiO_3$ interface, Phys. Rev. Lett. **119**, 237002 (2017).

[53] A. M. R. V. L. Monteiro, M. Vivek, D. J. Groenendijk, P. Bruneel, I. Leermakers, U. Zeitler, M. Gabay, and A. D. Caviglia, Band inversion driven by electronic correlations at the (111) $LaAlO_3/SrTiO_3$ interface, Phys. Rev. B **99**, 201102(R) (2019).

[54] F. Casola, T. van der Sar, and A. Yacoby, Probing condensed matter physics with magnetometry based on nitrogen-vacancy centres in diamond, Nat. Rev. Mater. **3**, 17088 (2018).

[55] L. Ella, A. Rozen, J. Birkbeck, M. Ben-Shalom, D. Perello, J. Zultak, T. Taniguchi, K. Watanabe, A. K. Geim, S. Ilani, and J. A. Sulpizio, Simultaneous voltage and current density imaging of flowing electrons in two dimensions, Nat. Nanotechnol. **14**, 480 (2019).

[56] P. Muralt and D. W. Pohl, Scanning tunneling potentiometry, Appl. Phys. Lett. **48**, 514 (1986).

[57] J. Martin, N. Akerman, G. Ulbricht, T. Lohmann, J. H. Smet, K. von Klitzing, and A. Yacoby, Observation of electron–hole puddles in graphene using a scanning single-electron transistor, Nat. Phys. **4**, 144 (2008).

[58] J. Waissman, M. Honig, S. Pecker, A. Benyamini, A. Hamo, and S. Ilani, Realization of pristine and locally tunable one-dimensional electron systems in carbon nanotubes, Nat. Nanotechnol. **8**, 569 (2013).

[59] G. Sala, H. Wang, W. Legrand, and P. Gambardella, Orbital Hanle magnetoresistance in a 3*d* transition metal, Phys. Rev. Lett. **131**, 156703 (2023).

[60] Y.-G. Choi, D. Jo, K.-H. Ko, D. Go, K.-H. Kim, H. G. Park, C. Kim, B.-C. Min, G.-M. Choi, and H.-W. Lee, Observation of the orbital Hall effect in a light metal Ti, Nature (London) **619**, 52 (2023).

[61] M. Serlin, C. L. Tschirhart, H. Polshyn, Y. Zhang, J. Zhu, K. Watanabe, T. Taniguchi, L. Balents, and A. F. Young, Intrinsic quantized anomalous Hall effect in a moiré heterostructure, Science **367**, 900 (2020).

[62] Z. Lu, T. Han, Y. Yao, Z. Hadjri, J. Yang, J. Seo, L. Shi, S. Ye, K. Watanabe, T. Taniguchi, and L. Ju, Extended quantum anomalous Hall states in graphene/hBN moiré superlattices, Nature (London) **637**, 1090 (2025).

[63] J.-X. Lin, Y.-H. Zhang, E. Morissette, Z. Wang, S. Liu, D. Rhodes, K. Watanabe, T. Taniguchi, J. Hone, and J. I. A. Li, Spin-orbit-driven ferromagnetism at half moiré filling in magic-angle twisted bilayer graphene, Science **375**, 437 (2022).

[64] L. Veyrat, C. Déprez, A. Coissard, X. Li, F. Gay, K. Watanabe, T. Taniguchi, Z. Han, B. A. Piot, H. Sellier, and B. Sacépé, Helical quantum Hall phase in graphene on $SrTiO_3$, Science **367**, 781 (2020).

[65] X. Gao, A. Jimeno-Pozo, P. A. Pantaleon, A. Rajesh, E. Codecido, D. L. Sharifi, Z. Zhang, Y. Liu, K. Watanabe, T. Taniguchi, M. W. Bockrath, F. Guinea, and C. N. Lau, Double-edged role of interactions in superconducting twisted bilayer graphene, Nat. Phys. **22**, 692 (2026).

[66] B. J. Roth, N. G. Sepulveda, and J. P. Wikswo, Using a magnetometer to image a two-dimensional current distribution, J. Appl. Phys. **65**, 361 (1989).

[67] K. C. Nowack, E. M. Spanton, M. Baenninger, M. König, J. R. Kirtley, B. Kalisky, C. Ames, P. Leubner, C. Brüne, H. Buhmann, L. W. Molenkamp, D. Goldhaber-Gordon, and K. A. Moler, Imaging currents in HgTe quantum wells in the quantum spin Hall regime, Nat. Mater. **12**, 787 (2013).